A search for distant radio galaxies from SUMSS and NVSS - I. Sample definition, radio and K-band imaging

Carlos de Breuck, Richard W. Hunstead, Elaine M. Sadler, Brigitte Rocca-Volmerange, Ilana Klamer

Mon. Not. R. Astron. Soc. **347,** 837–853 (2004)

A search for distant radio galaxies from SUMSS and NVSS – I. Sample definition, radio and *K*-band imaging

Carlos De Breuck,[1]★† Richard W. Hunstead,[2] Elaine M. Sadler,[2] Brigitte Rocca-Volmerange[1] and Ilana Klamer[2]

[1]*Institut d'Astrophysique de Paris, 98bis Boulevard Arago, 75014 Paris, France*
[2]*School of Physics, University of Sydney, NSW 2006, Australia*

Accepted 2003 October 1. Received 2003 September 26; in original form 2003 June 17

ABSTRACT

We present the first results from a pilot study to search for distant radio galaxies in the southern hemisphere ($\delta < -32^\circ$). Within a 360 deg^2 region of sky, we define a sample of 76 ultra-steep spectrum (USS) radio sources from the 843-MHz Sydney University Molonglo Sky Survey (SUMSS) and 1.4-GHz NRAO VLA Sky Survey (NVSS) radio surveys with $\alpha_{843}^{1400} < -1.3$ and $S_{1400} > 15$ mJy. We observed 71 sources without bright optical or near-infrared counterparts at 1.385 GHz with the ATCA, providing ∼5 arcsec resolution images and subarcsec positional accuracy. To identify their host galaxies, we obtained near-infrared *K*-band images with IRIS2 at the AAT and SofI at the NTT. We identify 92 per cent of the USS sources down to $K \sim 20.5$. The SUMSS–NVSS USS sources have a surface density more than 4 times higher than USS sources selected at lower frequencies. This is due to the higher effective selection frequency, and the well-matched resolutions of both surveys constructed using the same source fitting algorithm. The scattering of $\alpha > -1.3$ sources into the USS sample due to spectral index uncertainties can account for only 35 per cent of the observed USS sources. Because our sample appears to contain a similar fraction of very distant ($z > 3$) galaxies, selecting USS sources from SUMSS–NVSS should allow us to identify large numbers of massive galaxies at high redshift.

Key words: surveys – galaxies: active – radio continuum: galaxies – radio continuum: general.

1 INTRODUCTION

High-redshift radio galaxies (HzRGs) provide an ideal opportunity to study the early universe and gain insights into the formation and evolution of massive galaxies. The well known Hubble *K*–*z* relation (e.g. Lilly & Longair 1984; De Breuck et al. 2002) establishes that at $z \gtrsim 1$, radio galaxies can be used to trace the most massive star-forming populations. Thanks to the large sky coverage of present-day radio surveys, we can find the rare sources $\gtrsim$2 mag more luminous than similar redshift sources found in optical/near-infrared surveys. Together with the evolutionary path tracing HzRGs to low-redshift ($z \leqslant 1$) elliptical galaxies (e.g. Franceschini, Vercellone & Fabian 1998; Sadler 2003; Dunlop 2003) and the imperative that radio galaxies harbour central supermassive black holes (SMBHs), HzRGs are excellent laboratories for studying the earliest, most massive stellar systems.

HzRGs show diffuse morphologies with strong evidence supporting high star-formation rates (De Breuck et al. 2003; van Breugel et al. 1999b), starkly different to their low-redshift counterparts which are massive elliptical galaxies with little or no star formation. However, with only 26 HzRGs known at $z > 3$, the statistics are still unreliable. Addressing this issue is a major concern in our study. The search for HzRGs will also constrain formation mechanisms for SMBHs which are still very uncertain (e.g. Loeb 1993; Dunlop et al. 2003). A SMBH at $z > 5$ already implies that if its SMBH is not primordial, then it must form within <1.3 Gyr (for $\Omega_m = 0.27$, $\Omega_\Lambda = 0.73$, $H_0 = 71$ km s^{-1} Mpc^{-1}; Spergel et al. 2003; Tony et al. 2003). Only one HzRG is known at $z > 5$ (van Breugel et al. 1999a), and it is unclear whether HzRGs exist at earlier times. Clearly, the discovery of more HzRGs will dramatically increase our knowledge of galaxy formation and SMBH formation time-scales.

Although the large optical and infrared (IR) telescopes which probe the distant Universe are increasingly concentrated in the southern hemisphere, the search for HzRGs has until recently been limited to the northern hemisphere because of a lack of sensitive radio imaging surveys in the south. This has been rectified with near completion of the Sydney University Molonglo Sky Survey

★E-mail: cdebreuc@eso.org
†Present address: European Southern Observatory, Karl Schwarzschild Straße 2, D-85748 Garching, Germany.

(SUMSS; Bock, Large & Sadler 1999) at 843 MHz which will be used, together with its forerunner the 408-MHz Molonglo Reference Catalogue (MRC; Large et al. 1981), to search for the highest-redshift radio galaxies in the south. In this paper we present the results of a pilot study from SUMSS and the 1.4-GHz NRAO VLA Sky Survey (NVSS; Condon et al. 1998).

Our search for HzRGs consists of four steps: (i) definition of the sample, (ii) high-resolution radio imaging to obtain accurate positions and morphological information, (iii) near-IR identifications of the host galaxies, and (iv) optical and/or near-IR spectroscopy to measure their redshifts. Here we present the results from the first three steps of our program.

2 SAMPLE DEFINITION

We used the 2001 November 23 pre-release version of the SUMSS catalogue (Mauch et al. 2003) and version 39 of the NVSS catalogue (Condon et al. 1998) to construct a sample of ultra-steep spectrum (USS) sources. Note that this is a preliminary version of the SUMSS catalogue which has some differences (see below) from the first publicly released version, version 1.0 of 2003 February 25. The overlapping area with NVSS comprises 29 SUMSS mosaics of $4^\circ \times 4\overset{\circ}{.}3$ each. Because we only consider sources with $\delta < -32^\circ$ (see Section 3.1), the total sky area of our USS sample is 0.11 sr, or 360 deg^2. This area lies at $b < -31^\circ$, so Galactic extinction should not be a problem in identifying the host galaxies.

To determine which search radius to adopt in our catalogue correlation, we plotted the density of NVSS sources around SUMSS sources as a function of search radius (Fig. 1). We compared this distribution with the expected contribution from random correlations. To create a random position catalogue, we shifted the NVSS positions by 1° in declination. This comparison indicates that at search radii >40 arcsec, there are no more correlations than expected from a random distribution. Because we want our USS sample to be reliable, we used a 10-arcsec search radius. From Fig. 1, we find that the density of NVSS sources at offsets of 10 arcsec is $\sim 100\times$ higher than the random distribution, so we expect <1 chance coincidence between a SUMSS and NVSS source in our sample of 76 sources. Using this cut-off, we exclude the 2.8 per cent real sources with offsets >10 arcsec.

The difference in resolution between SUMSS (45 arcsec × 45 cosec$|\delta|$ arcsec) and NVSS (45 arcsec × 45 arcsec) may cause a source to be resolved into two or more components in one catalogue, but not in the other.[1] As this would lead to spuriously steep spectral indices, we excluded those objects which had another source within 100 arcsec, which corresponds to 24 per cent of the matched sample. This results in 9556 matches. The NVSS positions are expected to be more accurate than the SUMSS positions in this declination zone,[2] so we refer to the sources in common by their NVSS name in the standard IAU format.

We used a spectral index[3] cut-off $\alpha_{843}^{1400} < -1.3$, calculated using the integrated SUMSS flux densities from the preliminary catalogue. We also imposed a flux limit of $S_{1400} \geqslant 15$ mJy to increase the accuracy of the spectral indices. Of the 78 sources thus selected, we excluded two (NVSS J000920−351354 and NVSS J012653−322807)

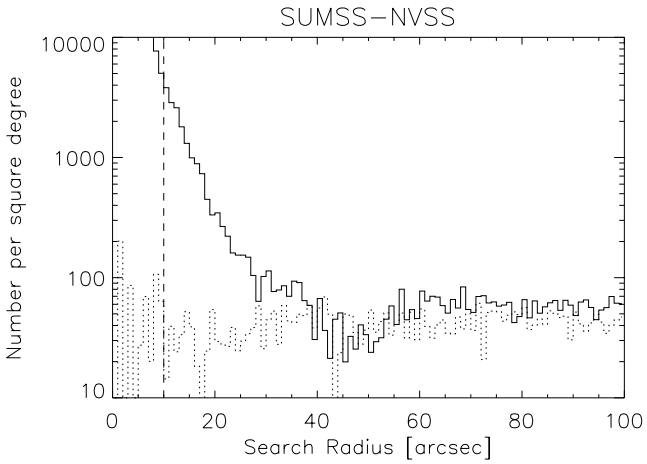

Figure 1. The local density of NVSS sources around SUMSS sources as a function of search radius. The dotted histogram represents the distribution of random associations (see text), and flattens off near the average source density in the NVSS survey. The vertical dashed line is the search radius adopted for our USS sample.

which have bright foreground stars in the field, as this complicates optical and near-IR imaging. The final sample of 76 sources is listed in Table 1.

Note that 23 sources in our sample have spectral indices $\alpha_{843}^{1400} > -1.3$, and nominally fall outside our selection criterion. This is because in Table 1 we have used the integrated flux densities from version 1.0 of the SUMSS catalogue. This version calculates the integrated flux densities from the peak intensity and the widths of the gaussian fit using the same method as described by Condon et al. (1998), while the preliminary version uses the raw output from the AIPS task VSAD (T. Mauch, private communication). We have manually checked the integrated flux densities of all 76 sources directly from the SUMSS images, and conclude that the values in the version 1.0 catalogue are reliable (there is no systematic difference, and no sources deviate by more than 25 per cent). The difference between the integrated flux densities appears to be most significant for the largest radio sources (using radio sizes determined from our ATCA imaging, see Section 3.1), confirming that the preliminary catalogue systematically overestimated the integrated flux density. Such errors show up easily in USS samples, as we select the sources with the largest differences between the SUMSS and NVSS flux densities. In the following, we shall therefore only use the integrated flux densities from the version 1.0 catalogue. This implies that our sample contains only 53 real USS sources with $\alpha_{843}^{1400} < -1.3$. We have decided to retain the other 23 sources to provide a baseline in spectral index and radio size against which to search for correlations with other properties (e.g. *K*-band magnitude, redshift) in our sample.

When using version 1.0 of the SUMSS catalogue, we find a total of 212 sources with $\alpha_{843}^{1400} < -1.3$. Of these sources, 69 are in new fields since added to the SUMSS coverage. The remaining 143 sources are all within the same fields, and qualify as USS sources due to the revised determination of the SUMSS flux density. Most of these sources have just made it into the USS cut-off: the median spectral index of the 90 'new' sources is $\bar{\alpha}_{843}^{1400} = -1.37$, while for the 53 USS sources in this paper, $\bar{\alpha}_{843}^{1400} = -1.56$. Because this new version of the SUMSS catalogue became available only after our radio and near-IR observations, these 'new' sources are not considered here.

[1] This can explain the small dip in the source density of Fig. 1 between search radii of 40 and 55 arcsec.

[2] At Dec. -32°, the SUMSS beam is 45×81 arcsec^2, i.e. significantly larger than the NVSS beam in the north–south (N–S) direction.

[3] Spectral index α is defined by the power law $S_\nu \propto \nu^\alpha$.

Table 1. The SUMSS–NVSS USS sample. The entries are explained in Section 4.

(1) Name	(2) S_{843} (mJy)	(3) S_{1400} (mJy)	(4) S_{843}^{1400}	(5) LAS (arsec)	(6) PA (deg.)	(7) IR	(8) $K(2'')$ (mag)	(9) $K(4'')$ (mag)	(10) $K(8'')$ (mag)	(11) RA^{radio}_{J2000} hms	(12) DEC^{radio}_{J2000} ° ′ ″	(13) Pos	(14) RA^{K-band}_{J2000} hms	(15) DEC^{K-band}_{J2000} ° ′ ″	(16) z_{2df}
NVSS J001339–322445	286 ± 8	155.2 ± 4.7	−1.21 ± 0.09	...	...	2MASS	...	...	13.11 ± 0.24	00 13 39.36	−32 24 49.5	N	00 13 39.37	−32 24 44.8	0.2598
NVSS J002001–333408	34 ± 1	16.9 ± 0.7	−1.38 ± 0.13	12.0	38	AAT	18.64 ± 0.13	17.84 ± 0.12	17.83 ± 0.20	00 20 01.31	−33 34 03.8	A	00 20 01.07	−33 34 06.7	...
NVSS J002112–321208	38 ± 1	16.4 ± 0.7	−1.66 ± 0.13	<5	...	AAT	19.81 ± 0.26	19.29 ± 0.31	19.06 ± 0.49	00 21 12.56	−32 12 08.6	A	00 21 12.40	−32 12 10.1	...
NVSS J002131–342225	39 ± 2	18.0 ± 1.0	−1.57 ± 0.15	12.5	116	AAT	16.28 ± 0.06	15.58 ± 0.06	15.30 ± 0.06	00 21 31.25	−34 22 24.1	A	00 21 31.31	−34 22 22.6	...
NVSS J002219–360728	31 ± 1	15.5 ± 0.7	−1.39 ± 0.14	...	...	2MASS	...	...	$K > 14.2$	00 22 19.42	−36 07 28.9	N	...	...	...
NVSS J002352–332338	59 ± 2	33.8 ± 1.5	−1.10 ± 0.13	37.3	79	AAT	19.76 ± 0.24	19.23 ± 0.29	18.44 ± 0.29	00 23 52.68	−33 23 38.2	N	00 23 53.29	−33 23 34.8	...
NVSS J002359–325756	503 ± 15	213.1 ± 7.6	−1.69 ± 0.09	10.1	94	AAT	19.40 ± 0.21	18.46 ± 0.19	18.67 ± 0.41	00 23 59.48	−32 57 55.3	A	00 23 59.42	−32 57 56.9	...
NVSS J002402–325253	100 ± 4	41.3 ± 1.3	−1.74 ± 0.10	3.8	4	AAT	20.05 ± 0.31	18.84 ± 0.22	18.97 ± 0.46	00 24 02.34	−32 52 55.8	A	00 24 02.29	−32 52 54.7	...
NVSS J002415–324102	97 ± 3	39.5 ± 1.3	−1.78 ± 0.10	<5	...	AAT	20.05 ± 0.32	19.50 ± 0.37	18.84 ± 0.42	00 24 15.08	−32 41 00.4	A	00 24 15.09	−32 41 02.4	...
NVSS J002427–325135	115 ± 4	53.0 ± 2.0	−1.54 ± 0.11	6.6	171	AAT	18.83 ± 0.14	18.09 ± 0.14	17.71 ± 0.18	00 24 27.76	−32 51 35.3	A	00 24 27.72	−32 51 35.8	...
NVSS J002627–323653	105 ± 4	44.4 ± 1.7	−1.72 ± 0.11	...	...	2MAAS	...	...	$K > 14.2$	00 26 27.94	−32 36 53.7	N	...	...	...
NVSS J002738–323501	35 ± 2	16.0 ± 1.1	−1.59 ± 0.20	45.5	23	NTT	18.75 ± 0.20	18.43 ± 0.19	18.24 ± 0.20	00 27 38.56	−32 34 56.3	N	00 27 38.58	−32 34 55.0	...
NVSS J011032–355445	37 ± 2	17.4 ± 0.7	−1.52 ± 0.16	<5	...	AAT	19.11 ± 0.17	18.73 ± 0.21	18.19 ± 0.25	01 10 32.05	−33 54 42.2	A	01 10 32.00	−33 54 42.8	...
NVSS J011606–331241	52 ± 2	22.1 ± 0.8	−1.70 ± 0.12	<6	...	NTT	19.05 ± 0.22	18.58 ± 0.20	18.09 ± 0.18	01 16 06.68	−33 12 42.6	A	01 16 06.77	−33 12 42.8	...
NVSS J011643–323415	24 ± 3	15.1 ± 1.4	−0.93 ± 0.33	42.3	121	AAT	18.85 ± 0.15	18.20 ± 0.16	18.09 ± 0.25	01 16 43.56	−32 34 15.9	N	01 16 43.53	−32 34 19.2	...
NVSS J012904–324815	77 ± 3	40.5 ± 1.7	−1.28 ± 0.12	...	...	2MASS	...	...	12.72 ± 0.13	01 29 04.52	−32 48 15.0	N	01 29 04.25	−32 48 13.1	0.180
NVSS J014413–330457	24 ± 2	16.0 ± 1.2	−0.82 ± 0.27	41.9	97	NTT	19.56 ± 0.27	18.90 ± 0.22	19.20 ± 0.29	01 44 12.98	−33 05 04.3	A	01 44 12.33	−33 05 00.1	...
NVSS J014529–325915	33 ± 2	17.3 ± 0.7	−1.32 ± 0.15	15.3	41	AAT	17.01 ± 0.07	16.20 ± 0.07	15.82 ± 0.07	01 45 29.38	−32 59 15.0	N	01 45 29.59	−32 59 16.9	...
NVSS J015223–333833	43 ± 2	17.3 ± 0.7	−1.81 ± 0.14	14.9	164	AAT	19.27 ± 0.19	18.91 ± 0.24	17.99 ± 0.23	01 52 22.83	−33 38 33.1	A	01 52 22.93	−33 38 36.2	...
NVSS J015232–333952	482 ± 14	247.3 ± 8.7	−1.32 ± 0.09	11.1	7	AAT	17.31 ± 0.08	16.65 ± 0.08	16.25 ± 0.08	01 52 32.27	−33 39 53.9	A	01 52 32.42	−33 39 55.4	...
NVSS J015324–334117	36 ± 2	19.8 ± 0.8	−1.23 ± 0.15	26.5	91	AAT	15.61 ± 0.06	14.74 ± 0.06	14.27 ± 0.06	01 53 24.37	−33 41 16.4	A	01 53 24.88	−33 41 23.5	0.1525
NVSS J015418–330150	33 ± 1	17.8 ± 0.7	−1.23 ± 0.13	<6	...	AAT	20.30 ± 0.36	20.21 ± 0.62	19.81 ± 0.88	01 54 18.20	−33 01 51.4	A	01 54 18.27	−33 01 50.7	...
NVSS J015436–333425	47 ± 2	21.2 ± 0.8	−1.59 ± 0.12	<6	...	NTT	19.84 ± 0.31	19.02 ± 0.23	18.19 ± 0.18	01 54 36.33	−33 34 24.9	A	01 54 36.37	−33 34 25.3	...
NVSS J015544–330633	69 ± 2	39.0 ± 1.6	−1.14 ± 0.11	18.6	115	AAT	17.86 ± 0.09	17.16 ± 0.09	16.95 ± 0.11	01 55 44.16	−33 06 33.8	A	01 55 44.60	−33 06 34.8	...
NVSS J021308–322338	61 ± 2	30.0 ± 1.0	−1.42 ± 0.11	<5	...	AAT	19.58 ± 0.18	19.04 ± 0.21	19.45 ± 0.56	02 13 08.06	−32 23 39.8	A	02 13 07.94	−32 23 40.2	...
NVSS J021359–321115	33 ± 2	17.4 ± 0.7	−1.29 ± 0.15	<6	...	AAT	18.56 ± 0.12	17.95 ± 0.13	18.01 ± 0.22	02 13 58.90	−32 11 17.0	A	02 13 58.91	−32 11 16.7	...
NVSS J021545–321047	108 ± 4	48.5 ± 1.5	−1.59 ± 0.10	7.5	98	AAT	19.28 ± 0.18	18.73 ± 0.20	18.86 ± 0.41	02 15 45.59	−32 10 46.9	A	02 15 45.48	−32 10 47.3	...
NVSS J021716–325121	47 ± 2	22.1 ± 0.8	−1.52 ± 0.12	4.1	44	AAT	19.37 ± 0.21	19.09 ± 0.29	18.41 ± 0.32	02 17 16.09	−32 51 20.5	A	02 17 15.92	−32 51 21.3	...
NVSS J030639–330432	63 ± 2	27.0 ± 0.9	−1.70 ± 0.10	<5	...	AAT	18.67 ± 0.13	18.13 ± 0.14	17.78 ± 0.19	03 06 39.75	−33 04 32.8	A	03 06 39.80	−33 04 32.7	...
NVSS J202026–372823	72 ± 2	36.8 ± 1.2	−1.34 ± 0.10	<5	...	AAT	18.88 ± 0.14	18.47 ± 0.17	18.10 ± 0.23	20 20 26.95	−37 28 20.9	A	20 20 26.98	−37 28 21.0	...
NVSS J202140–373942	38 ± 1	19.5 ± 1.1	−1.34 ± 0.14	29.1	21	AAT	16.19 ± 0.06	15.65 ± 0.06	15.22 ± 0.06	20 21 40.50	−37 39 41.6	A	20 21 40.59	−37 39 40.2	...
NVSS J202518–355834	47 ± 1	21.4 ± 0.8	−1.55 ± 0.11	<6	...	AAT	19.63 ± 0.23	18.84 ± 0.22	18.21 ± 0.25	20 25 18.32	−35 58 32.5	A	20 25 18.34	−35 58 33.2	...
NVSS J202856–353709	168 ± 5	98.1 ± 3.7	−1.07 ± 0.10	35.8	129	AAT	17.66 ± 0.09	16.88 ± 0.08	16.58 ± 0.09	20 28 56.52	−35 37 08.8	A	20 28 56.77	−35 37 06.0	...
NVSS J202945–344812	99 ± 3	52.5 ± 2.0	−1.25 ± 0.10	18.9	167	NTT	17.84 ± 0.15	17.62 ± 0.14	17.33 ± 0.13	20 29 45.66	−34 48 10.3	A	20 29 45.82	−34 48 15.5	...
NVSS J204147–331731	32 ± 1	16.4 ± 0.7	−1.35 ± 0.13	4.2	168	AAT	17.92 ± 0.10	17.20 ± 0.09	16.92 ± 0.11	20 41 47.58	−33 17 29.1	A	20 41 47.59	−33 17 29.8	...
NVSS J204420–334948	46 ± 1	20.8 ± 0.8	−1.60 ± 0.11	3.5	15	NTT	...	>21	...	20 44 20.83	−33 49 50.6	A	...	...	...
NVSS J213510–333703	47 ± 2	22.5 ± 0.8	−1.46 ± 0.11	<3	...	AAT	19.81 ± 0.31	18.91 ± 0.28	18.57 ± 0.40	21 35 10.43	−33 37 03.8	A	21 35 10.42	−33 37 04.4	...
NVSS J225719–343954	88 ± 3	37.5 ± 1.2	−1.69 ± 0.09	<6	...	AAT	17.15 ± 0.08	16.69 ± 0.08	16.54 ± 0.09	22 57 19.63	−34 39 55.9	A	22 57 19.63	−34 39 54.6	...
NVSS J230035–363410	35 ± 1	15.2 ± 0.7	−1.67 ± 0.14	<5	...	NTT	20.72 ± 0.44	19.82 ± 0.33	19.88 ± 0.45	23 00 35.74	−36 34 09.0	A	23 00 35.88	−36 34 10.6	...
NVSS J230123–344656	45 ± 2	20.0 ± 0.8	−1.61 ± 0.14	<6	...	NTT	20.09 ± 0.34	19.65 ± 0.31	19.01 ± 0.28	23 01 23.56	−36 46 57.3	A	23 01 23.55	−36 46 56.0	...

Table 1 – *continued*

(1) Name	(2) S_{843} (mJy)	(3) S_{1400} (mJy)	(4) S_{843}^{1400}	(5) LAS (arsec)	(6) PA (deg.)	(7) IR	(8) $K(2'')$ (mag)	(9) $K(4'')$ (mag)	(10) $K(8'')$ (mag)	(11) RA_{J2000}^{radio} hms	(12) DEC_{J2000}^{radio} ° ′ ″	(13) Pos	(14) RA_{J2000}^{K-band} hms	(15) DEC_{J2000}^{K-band} ° ′ ″	(16) z_{2df}
NVSS J230203–340932	29 ± 1	15.2 ± 0.7	−1.31 ± 0.14	25.6	91	AAT	19.29 ± 0.6	18.81 ± 0.19	18.60 ± 0.30	23 02 03.05	−34 09 34.4	N	23 02 02.98	−34 09 33.6	...
NVSS J230404–372450	71 ± 3	38.3 ± 1.6	−1.24 ± 0.12	31.8	126	AAT	18.77 ± 0.14	17.82 ± 0.12	17.23 ± 0.14	23 04 03.81	−37 24 51.0	A	23 04 03.86	−37 24 47.9	...
NVSS J230527–360534	72 ± 2	31.3 ± 1.0	−1.64 ± 0.10	<3	...	NTT	...	>20.6	...	23 05 27.63	−36 05 34.6	A	...	...	...
NVSS J230822–325027	48 ± 2	20.9 ± 0.8	−1.68 ± 0.11	1.7	141	AAT	18.87 ± 0.14	18.47 ± 0.17	18.55 ± 0.33	23 08 22.74	−32 50 30.0	A	23 08 22.78	−32 50 28.9	...
NVSS J230846–334810	108 ± 3	63.1 ± 2.3	−1.07 ± 0.10	29.8	114	AAT	17.60 ± 0.08	16.99 ± 0.08	16.58 ± 0.09	23 08 46.90	−33 48 13.6	A	23 08 46.73	−33 48 12.4	...
NVSS J230954–365653	34 ± 1	19.3 ± 1.5	−1.15 ± 0.18	55.2	25	NTT	19.90 ± 0.30	19.62 ± 0.28	20.76 ± 0.67	23 09 54.42	−36 56 46.58	N	23 09 54.66	−36 56 54.7	...
NVSS J231016–363624	51 ± 2	24.1 ± 1.2	−1.48 ± 0.13	28.6	3	AAT	18.35 ± 0.06	14.74 ± 0.06	14.57 ± 0.05	23 10 16.92	−36 36 32.1	A	23 10 16.89	−36 36 33.1	...
NVSS J231144–362215	35 ± 1	18.1 ± 0.7	−1.32 ± 0.12	16.4	69	NTT	20.52 ± 0.42	20.24 ± 0.65	20.07 ± 0.72	23 11 45.21	−36 22 16.6	A	23 11 45.22	−36 22 15.4	...
NVSS J231229–371324	39 ± 1	19.4 ± 0.8	−1.40 ± 0.12	5.5	161	AAT	18.47 ± 0.12	17.75 ± 0.12	17.53 ± 0.17	23 12 29.04	−37 13 26.3	A	23 12 29.08	−37 13 25.6	...
NVSS J231311–361558	43 ± 2	32.7 ± 1.7	−0.54 ± 0.14	62.9	48	AAT	18.46 ± 0.11	17.78 ± 0.12	17.50 ± 0.15	23 13 11.31	−36 15 59.7	A	23 13 11.11	−36 15 58.4	...
NVSS J231317–352133	32 ± 1	16.5 ± 0.7	−1.35 ± 0.13	6.1	102	AAT	20.04 ± 0.29	19.18 ± 0.26	18.69 ± 0.34	23 13 17.47	−35 21 34.9	A	23 13 17.54	−35 21 34.0	...
NVSS J231335–370609	42 ± 1	22.9 ± 0.8	−1.21 ± 0.11	<6	...	AAT	19.29 ± 0.18	18.78 ± 0.20	18.38 ± 0.27	23 13 35.43	−37 06 12.8	A	23 13 35.42	−37 06 10.7	...
NVSS J231338–362708	35 ± 1	16.6 ± 0.7	−1.50 ± 0.12	10.7	123	NTT	19.70 ± 0.29	19.36 ± 0.27	19.23 ± 0.32	23 13 38.69	−36 27 11.0	A	23 13 38.37	−36 27 08.9	...
NVSS J231341–372504	28 ± 1	15.3 ± 1.0	−1.23 ± 0.18	45.2	155	AAT	18.32 ± 0.11	17.36 ± 0.10	16.97 ± 0.11	23 13 41.54	−37 25 03.0	A	23 13 41.69	−37 25 01.5	...
NVSS J231357–372413	83 ± 3	37.3 ± 1.2	−1.58 ± 0.10	2.0	47	AAT	18.18 ± 0.11	17.08 ± 0.09	16.52 ± 0.11	23 13 57.48	−37 24 15.2	A	23 13 57.42	−37 24 15.6	...
NVSS J231402–372925	260 ± 8	129.9 ± 3.9	−1.37 ± 0.08	4.3	48	AAT	19.43 ± 0.17	18.76 ± 0.17	18.61 ± 0.29	23 14 02.45	−37 29 27.9	A	23 14 02.42	−37 29 27.4	...
NVSS J231459–362859	37 ± 1	20.9 ± 0.8	−1.16 ± 0.11	9.7	16	AAT	19.81 ± 0.22	19.37 ± 0.28	18.85 ± 0.37	23 14 59.03	−36 29 01.4	A	23 14 59.06	−36 29 02.8	...
NVSS J231519–342710	45 ± 1	22.4 ± 0.8	−1.41 ± 0.11	20.2	106	AAT	19.00 ± 0.15	18.22 ± 0.15	17.97 ± 0.21	23 15 19.03	−34 27 11.1	A	23 15 19.54	−34 27 13.4	...
NVSS J231726–371443	133 ± 4	71.3 ± 2.2	−1.23 ± 0.09	13.7	19	NTT	19.52 ± 0.28	19.09 ± 0.26	18.45 ± 0.23	23 17 26.90	−37 14 44.0	A	23 17 26.90	−37 14 47.2	...
NVSS J231727–352606	116 ± 3	59.2 ± 1.8	−1.33 ± 0.09	4.3	124	NTT	...	>20.6	...	23 17 27.41	−35 26 07.1	A	...	...	...
NVSS J232001–363246	46 ± 3	16.7 ± 0.7	−2.01 ± 0.16	<6	...	NTT	20.70 ± 0.46	20.70 ± 0.60	19.92 ± 0.55	23 20 01.17	−36 32 46.8	N	23 20 01.27	−36 32 46.5	...
NVSS J232014–375100	74 ± 2	42.7 ± 2.2	−1.11 ± 0.13	44.8	128	AAT	18.33 ± 0.11	17.83 ± 0.13	17.55 ± 0.17	23 20 14.73	−37 51 00.9	N	23 20 14.40	−37 51 01.0	...
NVSS J232058–365157	103 ± 3	51.4 ± 1.6	−1.38 ± 0.09	<5	...	AAT	19.09 ± 0.16	18.56 ± 0.19	18.73 ± 0.38	23 20 58.25	−36 51 59.4	A	23 20 58.28	−36 51 59.7	...
NVSS J232100–360223	37 ± 2	15.1 ± 0.7	−1.77 ± 0.14	2.4	174	NTT	20.20 ± 0.38	20.02 ± 0.38	19.48 ± 0.65	23 21 00.74	−36 02 25.1	A	23 21 00.64	−36 02 24.8	...
NVSS J232219–355816	59 ± 2	23.1 ± 0.8	−1.87 ± 0.10	1.9	149	NTT	...	>20.6	...	23 22 19.66	−35 58 17.3	A	...	...	...
NVSS J232322–345250	31 ± 2	17.1 ± 0.7	−1.19 ± 0.15	<6	...	AAT	18.50 ± 0.12	17.63 ± 0.11	17.12 ± 0.12	23 23 22.95	−34 52 49.2	A	23 23 22.96	−34 52 49.1	...
NVSS J232408–353547	31 ± 2	16.3 ± 1.2	−1.30 ± 0.19	...	...	2MASS	...	...	13.40 ± 0.17	23 24 08.52	−35 35 47.9	N	23 24 08.62	−35 35 44.7	0.2011
NVSS J232602–350321	27 ± 2	16.8 ± 1.2	−0.94 ± 0.24	15.2	140	AAT	16.28 ± 0.06	15.25 ± 0.06	14.66 ± 0.06	23 26 01.70	−35 03 29.6	A	23 26 01.67	−35 03 27.5	...
NVSS J232651–370909	71 ± 2	32.5 ± 1.1	−1.56 ± 0.10	<4	...	AAT	19.81 ± 0.26	19.52 ± 0.37	19.27 ± 0.59	23 26 51.52	−37 09 10.5	A	23 26 51.44	−37 09 10.0	...
NVSS J232956–374534	49 ± 1	22.6 ± 0.8	−1.53 ± 0.10	<6	...	AAT	19.84 ± 0.25	18.86 ± 0.22	18.53 ± 0.31	23 29 56.54	−37 45 40.9	A	23 29 56.61	−37 45 39.1	...
NVSS J233558–362236	41 ± 2	22.1 ± 1.4	−1.24 ± 0.16	39.2	148	NTT	17.34 ± 0.13	16.94 ± 0.11	16.73 ± 0.11	23 35 58.72	−36 22 36.5	N	23 35 59.01	−36 22 41.6	...
NVSS J233729–355529	240 ± 7	123.0 ± 4.4	−1.33 ± 0.09	7.4	72	AAT	19.92 ± 0.28	19.20 ± 0.29	17.94 ± 0.21	23 37 29.98	−35 55 31.7	A	23 37 29.76	−35 55 29.0	...
NVSS J234137–342230	38 ± 1	17.4 ± 1.0	−1.55 ± 0.15	<6	...	NTT	...	>21	...	23 41 37.33	−34 22 32.9	A	...	...	...
NVSS J234145–350624	3523 ± 105	1823.2 ± 54.7	−1.30 ± 0.08	<5	...	AAT	17.95 ± 0.10	16.87 ± 0.09	16.25 ± 0.09	23 41 45.90	−35 06 23.4	A	23 41 45.85	−35 06 22.2	...
NVSS J234904–362451	90 ± 3	46.5 ± 1.8	−1.31 ± 0.10	9.5	137	AAT	19.47 ± 0.20	18.32 ± 0.15	17.64 ± 0.16	23 49 04.24	−36 24 53.4	A	23 49 04.28	−36 24 53.1	...
NVSS J235137–362632	85 ± 3	37.4 ± 1.5	−1.62 ± 0.11	3.9	10	NTT	...	>20.4	...	23 51 37.73	−36 26 35.1	A	...	...	...

2.1 Literature

We searched for obvious optical and K-band identifications at the NVSS positions using the Digitized Sky Survey (DSS) and the 2 Micron All Sky Survey (2MASS; Skrutskie et al. 1997). Of the five sources detected in the DSS, three were also seen in 2MASS. We did not obtain more accurate radio or K-band identifications for these sources, as they are likely to be located at low ($z \ll 1$) redshifts. As a result, we lack K-band information for two sources, and for these, we quote the 2MASS 10σ sensitivity limit. For the three sources detected in 2MASS, we quote their 'total magnitudes from fit extrapolation' and list these in column (10) of Table 1. Four sources have measured spectroscopic redshifts $0.15 < z < 0.26$ from the 2dF Galaxy Redshift Survey (2dFGRS; Colless et al. 2001); these are listed in column (13) of Table 1.

3 OBSERVATIONS AND DATA REDUCTION

3.1 ATCA

We used the Australia Telescope Compact Array (ATCA) over the period UT 2001 December 12–14 to measure accurate radio positions and morphologies of 71 sources in our USS sample. The 6A configuration was used, spanning baselines from 330 m to 6 km. We observed simultaneously at 1.344 and 1.432 GHz, and obtained 4–10 cuts of 3 min for each target, spread in hour angle. Primary flux calibration was based on observations of PKS B1934−638 and the phase calibrators were PKS B1933−400, B2341−351 and B0153−410. To avoid high azimuth tracking speeds, we excluded sources near the local zenith by limiting our sample to $\delta < -32^\circ$.

We used the CAONIS on-line data-reduction tool to determine if a source was detected with sufficient signal-to-noise ratio (S/N). Once a source had been clearly detected, and its morphology determined, we skipped to the next source, with the aim of obtaining a set of radio maps with a uniform S/N level and uv coverage. Table 2 gives the total on-source integration times for each source.

The resulting synthesized beam widths are ∼9 arcsec × 5 arcsec, and the positional accuracy is estimated to be <1 arcsec. We followed standard data reduction procedures in MIRIAD, and combined the 1.344 and 1.432 GHz uv data to increase the signal-to-noise and better sample the uv plane. The final images have a rms noise level of ∼ 0.4 mJy.

For approximately 30 per cent of our sample, positive K-band identifications were confused by several sources located near the

Table 2. Integration times for the radio and near-IR observations

Name	ATCA s	AAT s	NTT s	Name	ATCA s	AAT s	NTT s
NVSS J001339−322445	···	···	···	NVSS J230035−363410	720	896	2400
NVSS J002001−333408	3600	896	···	NVSS J230123−364656	900	896	2400
NVSS J002112−321208	900	896	···	NVSS J230203−340932	2376	1792	···
NVSS J002131−342225	900	896	···	NVSS J230404−372450	3924	896	···
NVSS J002219−360728	···	···	···	NVSS J230527−360534	2376	···	900
NVSS J002352−332338	2412	896	···	NVSS J230822−325027	900	896	···
NVSS J002359−325756	900	896	···	NVSS J230846−334810	1260	896	···
NVSS J002402−325253	720	896	···	NVSS J230954−365653	3924	896	1500
NVSS J002415−324102	900	896	···	NVSS J231016−363624	900	896	···
NVSS J002427−325135	900	896	···	NVSS J231144−362215	1260	1792	2400
NVSS J002627−323653	···	···	···	NVSS J231229−371324	900	896	···
NVSS J002738−323501	3348	896	1680	NVSS J231311−361558	900	896	···
NVSS J011032−335445	1080	896	···	NVSS J231317−352133	900	1792	···
NVSS J011606−331241	1080	896	2400	NVSS J231335−370609	900	896	···
NVSS J011643−323415	3564	896	···	NVSS J231338−362708	1260	896	2400
NVSS J012904−324815	···	···	···	NVSS J231341−372504	3564	896	···
NVSS J014413−330457	3240	896	2400	NVSS J231357−372413	1260	896	···
NVSS J014529−325915	720	1792	···	NVSS J231402−372925	900	896	···
NVSS J015223−333833	3240	1792	···	NVSS J231459−362859	900	896	···
NVSS J015232−333952	900	1792	···	NVSS J231519−342710	1620	896	···
NVSS J015324−334117	1080	896	···	NVSS J231726−371443	1260	1792	1260
NVSS J015418−330150	1260	896	···	NVSS J231727−352606	2556	896	2400
NVSS J015436−333425	1080	896	2400	NVSS J232001−363246	1800	896	1200
NVSS J015544−330633	900	896	···	NVSS J232014−375100	1260	896	···
NVSS J021308−322338	1260	1792	···	NVSS J232058−365157	1620	1344	···
NVSS J021359−321115	1260	896	···	NVSS J232100−360223	2376	896	1380
NVSS J021545−321047	1260	896	···	NVSS J232219−355816	2376	896	1800
NVSS J021716−325121	1260	896	···	NVSS J232322−345250	1440	896	···
NVSS J030639−330432	1440	896	···	NVSS J232408−353547	···	···	···
NVSS J202026−372823	1080	896	···	NVSS J232602−350321	1440	896	···
NVSS J202140−373942	1908	896	···	NVSS J232651−370909	900	896	···
NVSS J202518−355834	1440	1792	···	NVSS J232956−374534	720	896	···
NVSS J202856−353709	1260	896	···	NVSS J233558−362236	3600	896	1980
NVSS J202945−344812	1080	1792	2160	NVSS J233729−355529	720	896	···
NVSS J204147−331731	720	896	···	NVSS J234137−342230	2160	896	1980
NVSS J204420−334948	1908	2688	2400	NVSS J234145−350624	3000	896	···
NVSS J213510−333703	2160	2688	···	NVSS J234904−362451	1260	896	···
NVSS J225719−343954	900	576	···	NVSS J235137−362632	2628	896	2400

radio derived positions. We therefore obtained follow-up radio observations to increase the sensitivity of the previous images. We re-observed 20 USS sources on UT 2003 July 29–30 in the 6A configuration. We observed simultaneously at 1.384 and 2.368 GHz and obtained 7–8 cuts of 4–6 min for each target, spread over 12 hr in hour angle. The phase calibrators observed were PKS B1933−400, B2254−367, B0008−421 and B0153−410. All other parameters and data reduction techniques are as described above.

3.2 AAT

We obtained K_S band imaging of 70 sources from our sample on the nights of UT 2002 October 17 to 20, using the new IRIS2 instrument (Gillingham & Jones 2000) at the 3.9-m Anglo-Australian Telescope at Siding Spring Observatory. Conditions were mostly photometric, but the seeing was highly variable on some nights. This led to a loss of sensitivity of up to 2 mag when the K_S band seeing was 3.0 arcsec, as compared to good conditions with 1.0-arcsec seeing. We used typical integration times of 64 s, consisting of 8 co-adds of 8 s each in a 14-point random jitter pattern within a 40 arcsec × 40 arcsec box. The detector is a 1024 × 1024 HAWAII HgCdTe array, with a pixel scale of 0.446 arcsec pixel^{-1}, resulting in a ∼ 8 arcmin × 8 arcmin field of view.

We used the online data-reduction tool ORAC-DR (Cavanagh et al. 2003) to sky-subtract, register and sum our data. This allowed us to re-observe several of the sources which were not detected after the first 14-point dither pattern. This quick data reduction also allowed us to re-observe eight sources where we did not detect the object due to loss of sensitivity during periods of bad seeing. In our final data reduction, we retained only data obtained with a K_S band seeing <2.0 arcsec, except for six sources with $K < 18$.

3.3 NTT

For the 20 sources not detected in our AAT/IRIS2 images, we obtained deeper K_S band images on the nights of UT 2002 November 25 to 27 using the Son of Isaac (SofI) instrument (Moorwood, Cuby & Lidman 1998) at the ESO 3.5-m New Technology Telescope (NTT). Conditions were photometric with 0.7-arcsec seeing. We used typical integration times of 60 s, consisting of 6 co-adds of 10 s each in a 15- to 40-point random jitter pattern within 40 arcsec × 40 arcsec. The detector is a 1024 × 1024 HAWAII HgCdTe array, with a pixel scale of 0.292 arcsec pixel^{-1}, resulting in a ∼5 arcmin × 5 arcmin field of view.

We reduced the data using the NOAO IRAF package. After flat-fielding, the data were sky-subtracted, registered, and summed using the DIMSUM near-IR data reduction package. Because most images were observed with good seeing, we block-replicated the pixels by a factor of 2 before summing the individual images.

3.4 Astrometry

The combined images from the ORAC-DR and DIMSUM reductions contain a crude astrometrical solution based on the telescope pointings. We used the Skycat GAIA tool to identify the non-saturated ($12 < R < 18$) stars from USNO-A2.0 catalogue (Monet et al. 1998), and fine-tuned our astrometry accordingly. Because of the large field of view, we could identify on average ∼90 stars in each IRIS2 image, and ∼40 in the SofI images, allowing an accurate astrometrical solution including the rotation and stretch terms. The main uncertainty in the *relative* near-IR to radio astrometry stems from the uncertainty in the USNO-A2.0 catalogue, which is $1\sigma \approx$ 0.25 arcsec (Deutsch 1999). This is more accurate than our ATCA astrometry, and should therefore be sufficient to identify the K_S band counterparts of our USS sources.

3.5 Photometry

We calibrated the photometry using short observations of standard stars from the UKIRT faint standard list (Hawarden et al. 2001). This procedure yielded typical zero-points of $K_{S0} = 22.20 \pm 0.10$ for IRIS2, and $K_{S0} = 22.11 \pm 0.02$ for SofI (for 1 count s^{-1}, integrated over the source). Because our resulting images have a large field of view, they generally contain several stars which are also detected in the Deep Near Infrared Survey of the Southern Sky (DENIS Epchtein et al. 1997). We extracted all the DENIS stars in our images with reliable K-band photometry (confidence coefficient >75) from the catalogue constructed at the Paris Data Analysis Centre (G. Simon, private communication). A comparison with our photometry yields a small systematic offset of −0.06 mag in both the IRIS2 and SofI photometric zeropoints. We applied this correction to our photometry. We estimate the uncertainty in the zeropoints by comparing field stars observed by both telescopes, and find $\Delta(K_{S0}) \simeq 0.05$.

We did not correct for airmass variations, because most of our objects were observed with airmasses <1.7, and the airmass dependence in K_S band is small compared to the fitting errors described below. Similarly, the effect of Galactic extinction is expected to be negligible in our fields (located at $b < -31°$), and no correction has been applied. Note that all our near–IR observations used the K_S-band filter and not the standard K-band filter. We did not correct our magnitudes to K-band because we do not have any colour information, and the correction is expected to be much smaller than the photometric uncertainties. In the following, we shall for refer to the magnitudes as K-band to facilitate comparison with the literature.

We used the IRAF task PHOT to measure the magnitudes of the K-band identifications. To facilitate comparison with the literature, we use three different apertures, with diameters of 2.0, 4.0 and 8.0 arcsec. The uncertainties quoted are our best estimates, which include both the zero-point uncertainty and the fitting uncertainty given by the PHOT routine.

4 RESULTS

Table 1 lists our sample with the results from our radio and near-IR imaging. The columns are:

(1) The name of the source in IAU J2000 format.

(2) The integrated 843-MHz flux density from the SUMSS catalogue.

(3) The integrated 1.4-GHz flux density from the NVSS catalogue.

(4) The two-point spectral index between SUMSS and NVSS.

(5) The largest angular size, as determined from the ATCA maps. For single component sources, this is the de-convolved major axis of the elliptical Gaussian, or, for unresolved sources (preceded by <), an upper limit is given by the resolution. For multiple component sources, this is the largest possible separation between their components.

(6) The de-convolved position angle of the radio structure, as determined from the ATCA maps, measured north through east. For multiple component sources, this is the orientation of the most widely separated components used to calculate the LAS (col. 5).

(7) The telescope used to obtain the K-band imaging.

(8)–(10) The K-band magnitude determined in apertures with diameters of 2, 4 and 8 arcsec. For the 2MASS photometry, these are the total magnitudes from fit extrapolation.

(11)–(12) The J2000 coordinates of the radio source, either measured from the ATCA images or from the NVSS catalogue, as indicated in column (13). The positions in the ATCA maps have been fitted with a single two-dimensional elliptical Gaussian. For multiple component sources, the geometric midpoint is given, unless mentioned otherwise in the notes on individual sources.

(13) The origin of the radio position given in columns (11) and (12): A = ATCA image, N = NVSS catalogue.

(14) and (15) The J2000 coordinates of the K-band identification. (14) and (15).

(16) The spectroscopic redshift from the 2dFGRS.

Notes on individual sources are given in the Appendix. Fig. 2 shows overlays of the ATCA 1.4- or 2.4-GHz radio contours on to K-band images.

5 DISCUSSION

5.1 Correlations

We now examine the correlations between the different source parameters in our sample. Because 30 per cent of our sample contains sources with $\alpha_{843}^{1400} > -1.3$ and large radio sizes, we can study the dependence of K-band magnitude on these parameters. Fig. 3 shows that the K-band magnitude and radio spectral index are correlated. The generalized Spearman rank and generalized Kendall's tau coefficients (e.g. Isobe, Feigelson & Nelson 1986) suggest this relation is significant at the 99.95 per cent level. This correlation arises because both radio spectral index and K-band magnitude are correlated with redshift, reinforcing our approach of using K-band magnitude as an additional criterion for selecting the highest redshift candidates.

Several samples of USS sources (Blundell et al. 1998; Stern et al. 1999) have applied a radio angular-size cut-off to exclude large radio sources, which are thought to be at relatively low redshift. We can check the efficiency of this approach with our sample, as we have radio size information for 95 per cent of our sources, and K-band information to estimate their redshifts (see Section 5.3). Note that our sample also has an implicit angular size cut-off due to the exclusion of SUMSS sources with more than one NVSS source within 100 arcsec (see Section 2). Considering only the 53 sources with $\alpha_{843}^{1400} < -1.3$ and radio size information, there indeed appears to be a correlation between radio size and K-band magnitude (see Fig. 4). The generalized Spearman rank and Kendall's tau coefficients suggest that this correlation is significant at the 99.7 per cent level. Because our sample contains only 29 radio sources larger than 10 arcsec (of which only 12 have $\alpha_{843}^{1400} < -1.3$), we consider this suggestive, but not conclusive evidence that the most distant radio sources in our radio sample have smaller radio sizes. Nevertheless, it is remarkable that only two sources with $K(4\,\mathrm{arcsec}) > 19.5$ have a radio size larger than 6 arcsec. This suggests that a significant fraction of the compact steep spectrum sources in our sample are either at high redshift or are heavily obscured by dust (Reuland et al. 2003).

5.2 Surface density of USS sources

In this paper, we select USS sources on the basis of the radio spectral index between 843 and 1400 MHz. We now evaluate how well this works in comparison with the techniques used in earlier USS samples. There are two considerations here: the *number* of sources which this technique yields, and the *fraction* of USS sources which lie at high redshift.

Table 3 compares the results from our SUMSS–NVSS pilot study with earlier USS samples observed by De Breuck et al. (2002) and Jarvis et al. (2001). The SUMSS–NVSS USS selection yields a USS surface density more than four times higher than the WENSS–NVSS sample of De Breuck et al. (2002) at the same 1.4-GHz flux level. Note that due to the incompleteness of our USS sample (see Section 2), these numbers are strictly lower limits. There are several explanations for this higher density, as follows.

First, the higher *observed* selection frequency of 843 MHz compared to 325 MHz means that we are also sampling a higher *rest-frame* spectral index of the radio sources. Because most radio spectra of powerful radio galaxies and compact steep spectrum sources have a tendency to steepen towards higher frequencies (e.g. Gopal-Krishna 1988; Mangalam & Gopal-Krishna 1995; Athreya & Kapahi 1998; Murgia et al. 1999; Blundell, Rawlings & Willott 1999; De Breuck et al. 2000; Sohn, Klein & Mack 2003), we are effectively probing an intrinsically steeper part of the radio spectrum. Therefore, on average, $\alpha_{843}^{1400} = -1.3$ corresponds to $\alpha_{325}^{1400} > -1.3$. This slightly more relaxed cut-off leads to a fast increase in the number of USS selected sources (due to the steep tail of the spectral index distribution), but due to the other two effects described here, we cannot use this to estimate the α_{843}^{1400} cut-off equivalent to $\alpha_{325}^{1400} = -1.3$.

Secondly, the SUMSS and NVSS catalogues have both been constructed with the AIPS task VSAD (Condon et al. 1998; Mauch et al. 2003), while the WENSS survey uses an IDL-based fitting routine (Rengelink et al. 1997). Because both USS samples consider only isolated sources in both catalogues, the use of the same fitting routine in both surveys is more appropriate. For example, De Breuck et al. (2000) considered only 'single component' WENSS sources, which may well exclude a substantial fraction of real USS sources. Furthermore, the spatial resolution of SUMSS (45 arcsec $\times$ 45 cosec$|\delta|$ arcsec) is better matched to NVSS (45 arcsec $\times$ 45 arcsec) than that of WENSS (54 arcsec $\times$ 54 cosec$|\delta|$ arcsec), so fewer sources will be removed by our selection criterion to exclude sources resolved in only one of the two catalogues (see Section 2). The WENSS–NVSS USS sample is therefore less complete than the SUMSS–NVSS USS sample.

Thirdly, the shorter frequency baseline between SUMSS and NVSS leads to a median uncertainty in the derived USS spectral indices $\Delta\bar{\alpha}_{843}^{1400} = 0.12$, while for WENSS–NVSS this is $\Delta\bar{\alpha}_{325}^{1400} = 0.04$ (De Breuck et al. 2000). Because the $\alpha < -1.3$ cut-off is on the very steep tail of the spectral index distribution, we expect more sources with $\alpha > -1.3$ to scatter into into the USS sample than there will be $\alpha < -1.3$ scattering out. To estimate the magnitude of this effect, we have generated a random sample of sources drawn from the SUMSS–NVSS spectral index distribution, and added random spectral index uncertainties to this (Rengelink 1999). Here, we use the publicly released version of the SUMSS catalogue, containing 212 USS sources with $\alpha < -1.3$, to get a reliable estimate of this effect. Adopting a mean spectral index $\bar{\alpha} = -0.82$ and a standard deviation of $\sigma_\alpha = 0.25$, we expect that, due to uncertainties in the spectral indices in our sample, ~ 40 real $\alpha < -1.3$ have observed $\alpha > -1.3$, while ~ 115 real $\alpha > -1.3$ have observed $\alpha < -1.3$. Hence, this would lead to a surplus of $\sim$75 sources (35 per cent) in a USS sample (compared to $\sim$3 per cent in the WENSS–NVSS sample; De Breuck et al. 2000). However, we do not expect that this 'contamination' of $\alpha > -1.3$ sources will decrease

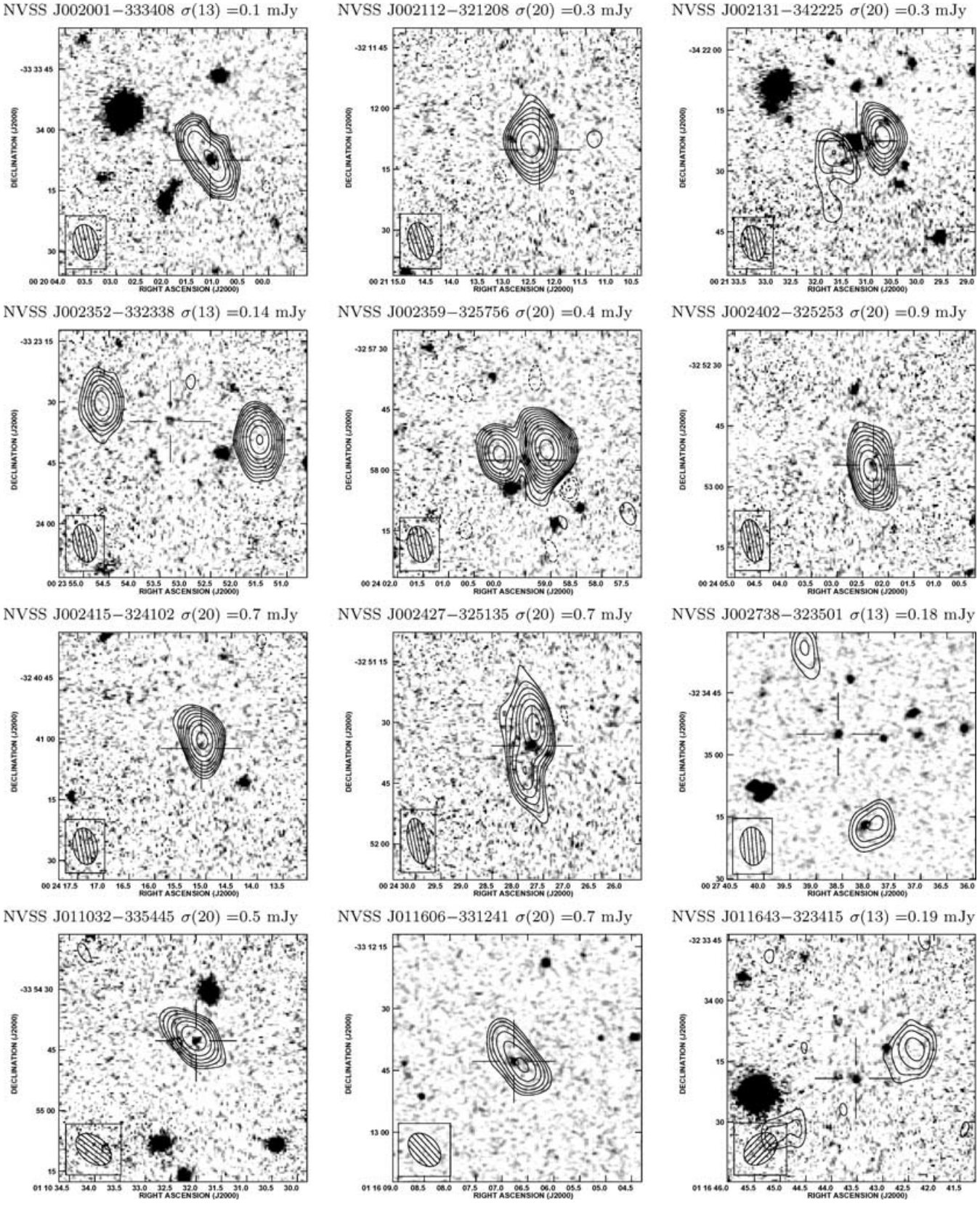

Figure 2. Overlays of ATCA 13- or 20-cm maps on AAT/IRIS2 or NTT/SofI K-band images. We have smoothed the SofI images using a circular 0.7-arcsec Gaussian, corresponding to the average seeing. The contour scheme is a geometric progression in $\sqrt{2}$, which implies a factor two change in surface brightness every 2 contours. The first contour level, indicated above each plot, is at $3\sigma_{\rm rms}$, where $\sigma_{\rm rms}$ is the rms noise measured around the sources. The wavelength of the radio map is given in brackets. The restoring beams are indicated in the lower left corner of the plots. The open cross indicates the K-band identification, as listed in Table 1.

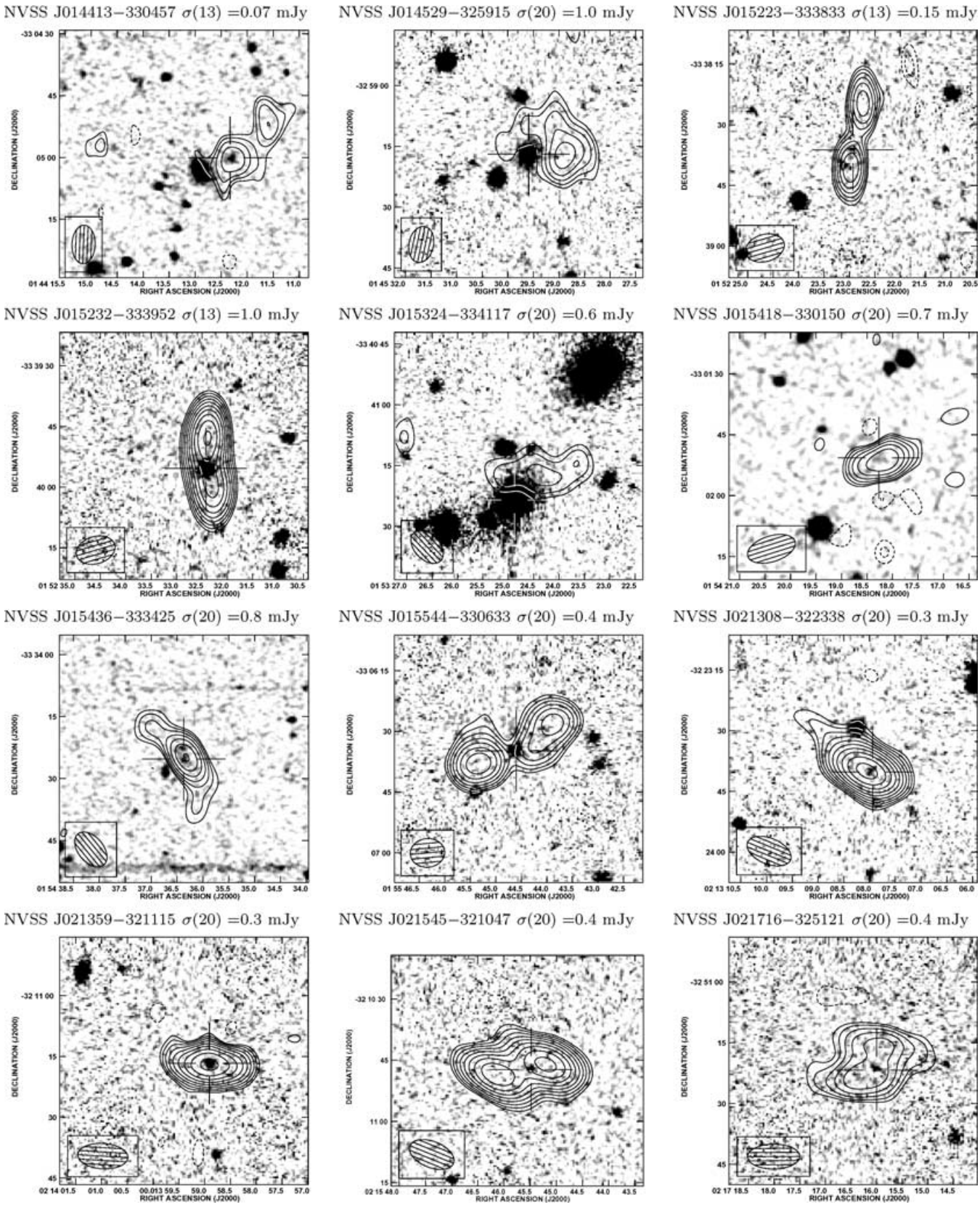

Figure 2 – *continued*

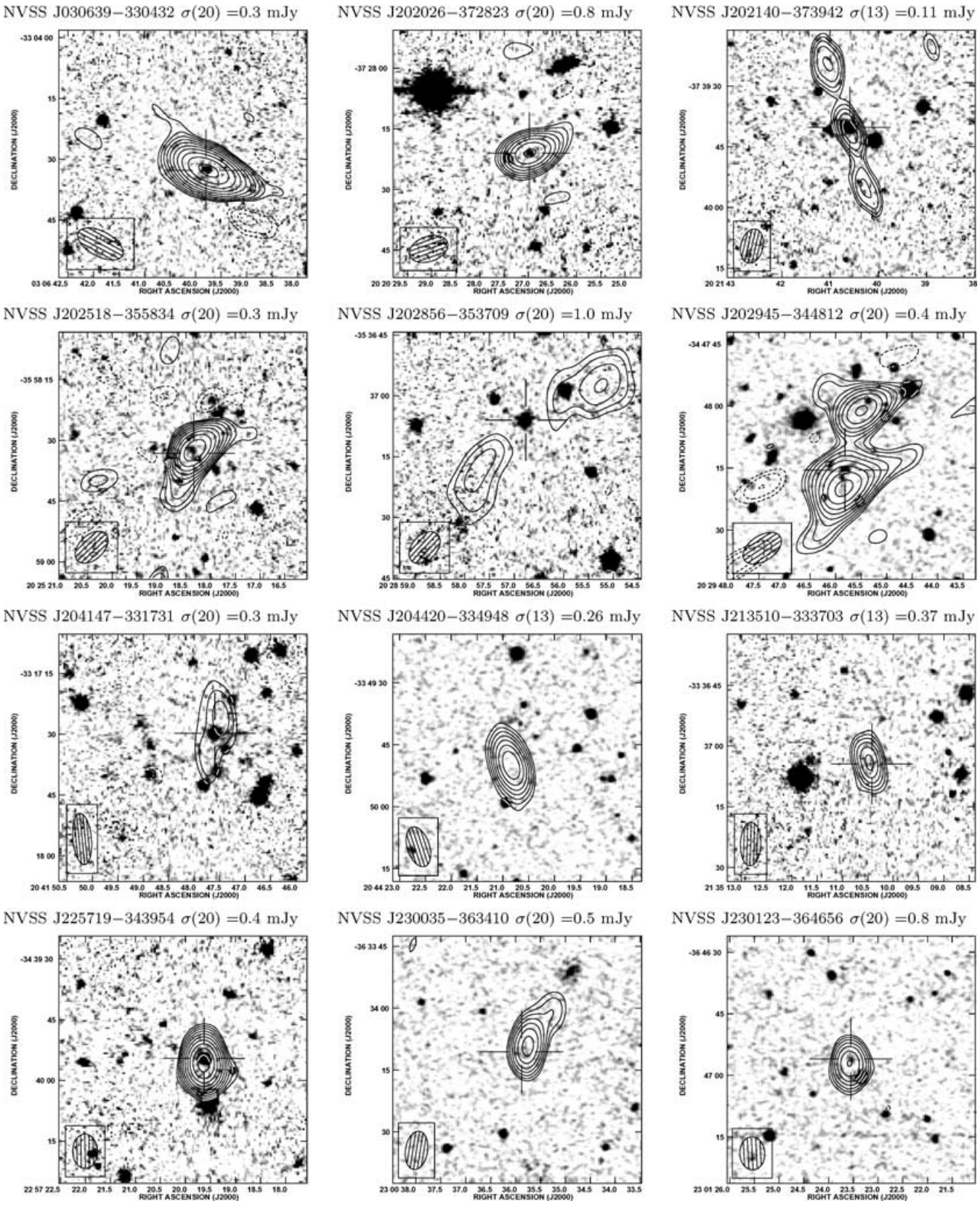

Figure 2 *– continued*

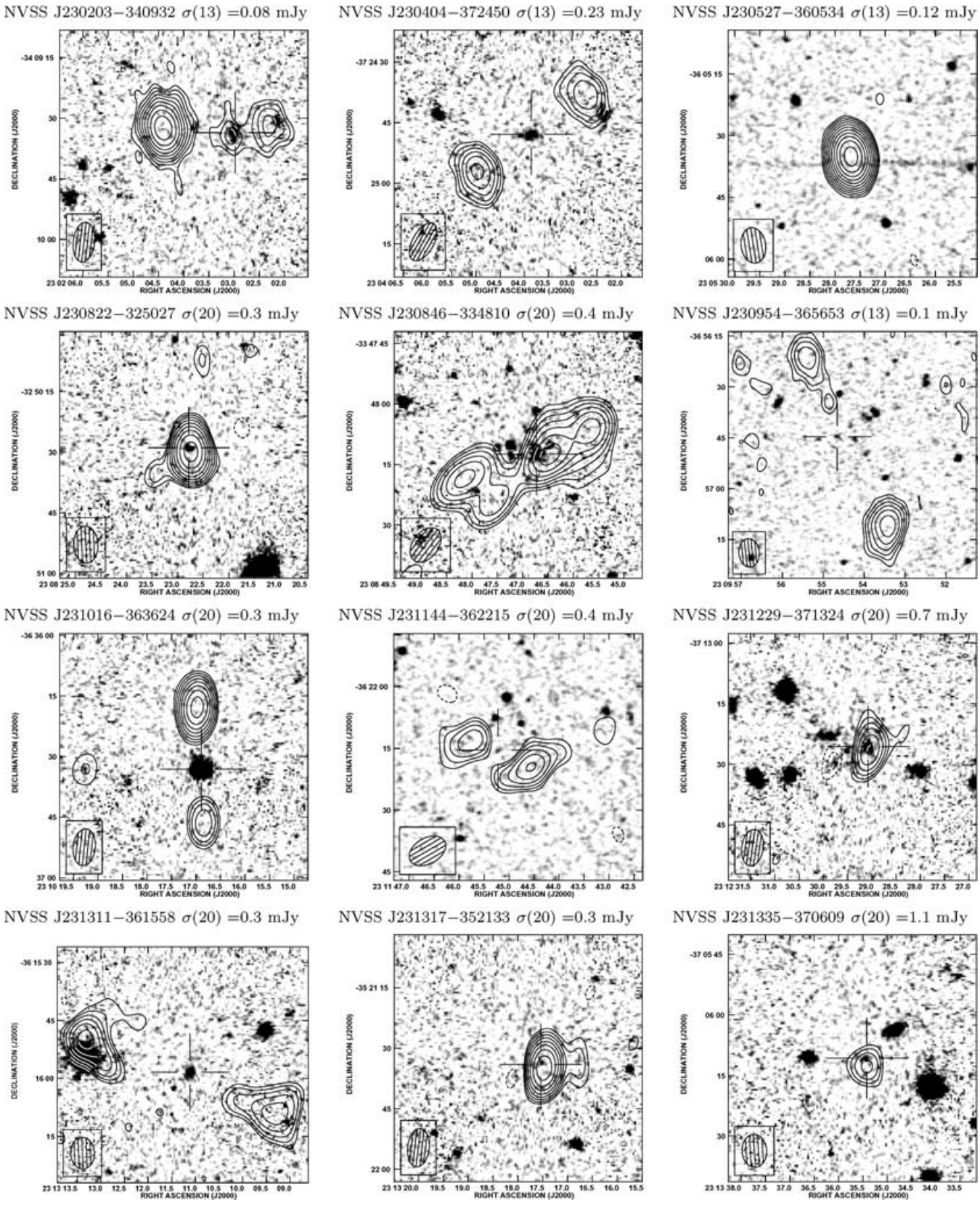

Figure 2 – *continued*

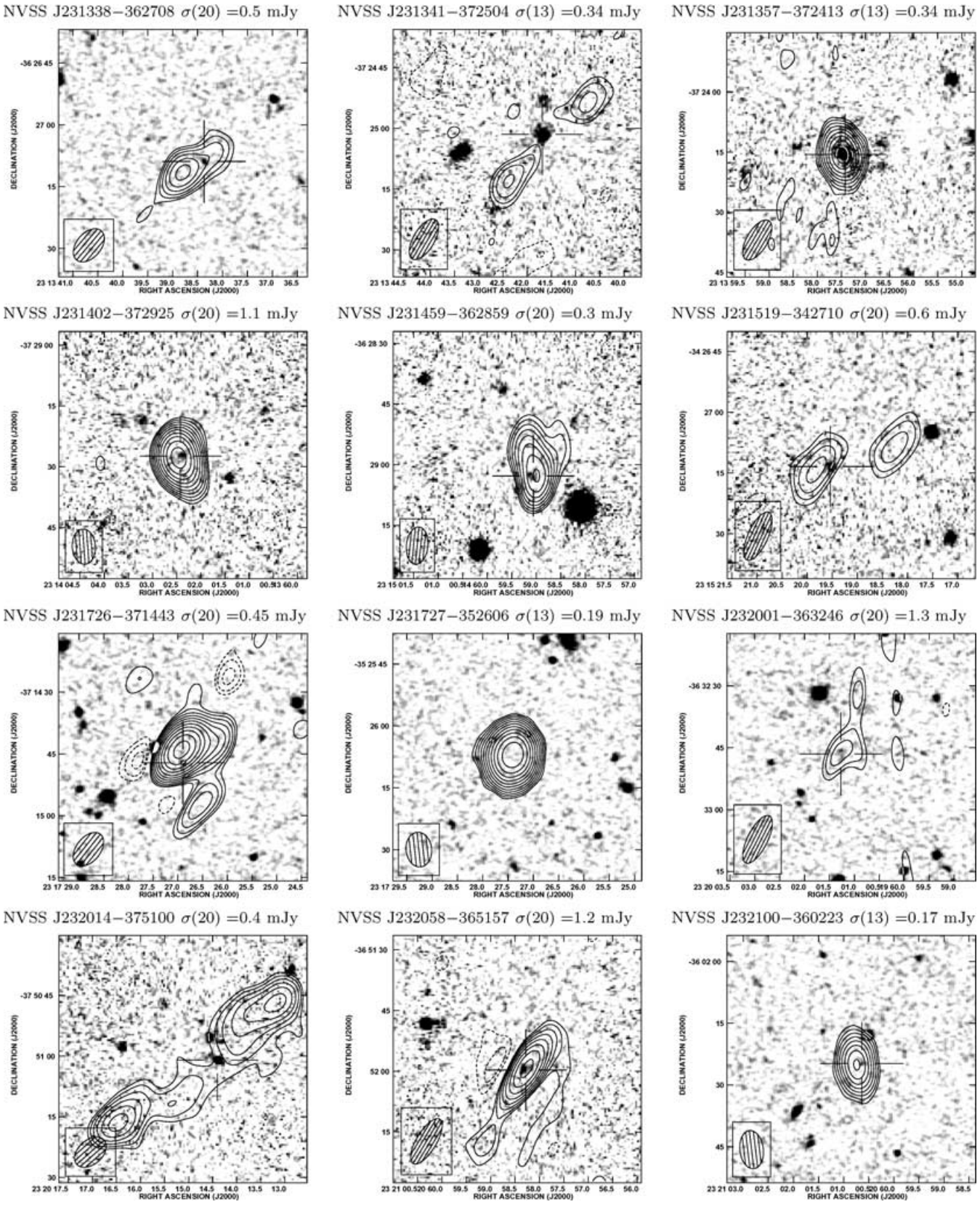

Figure 2 – *continued*

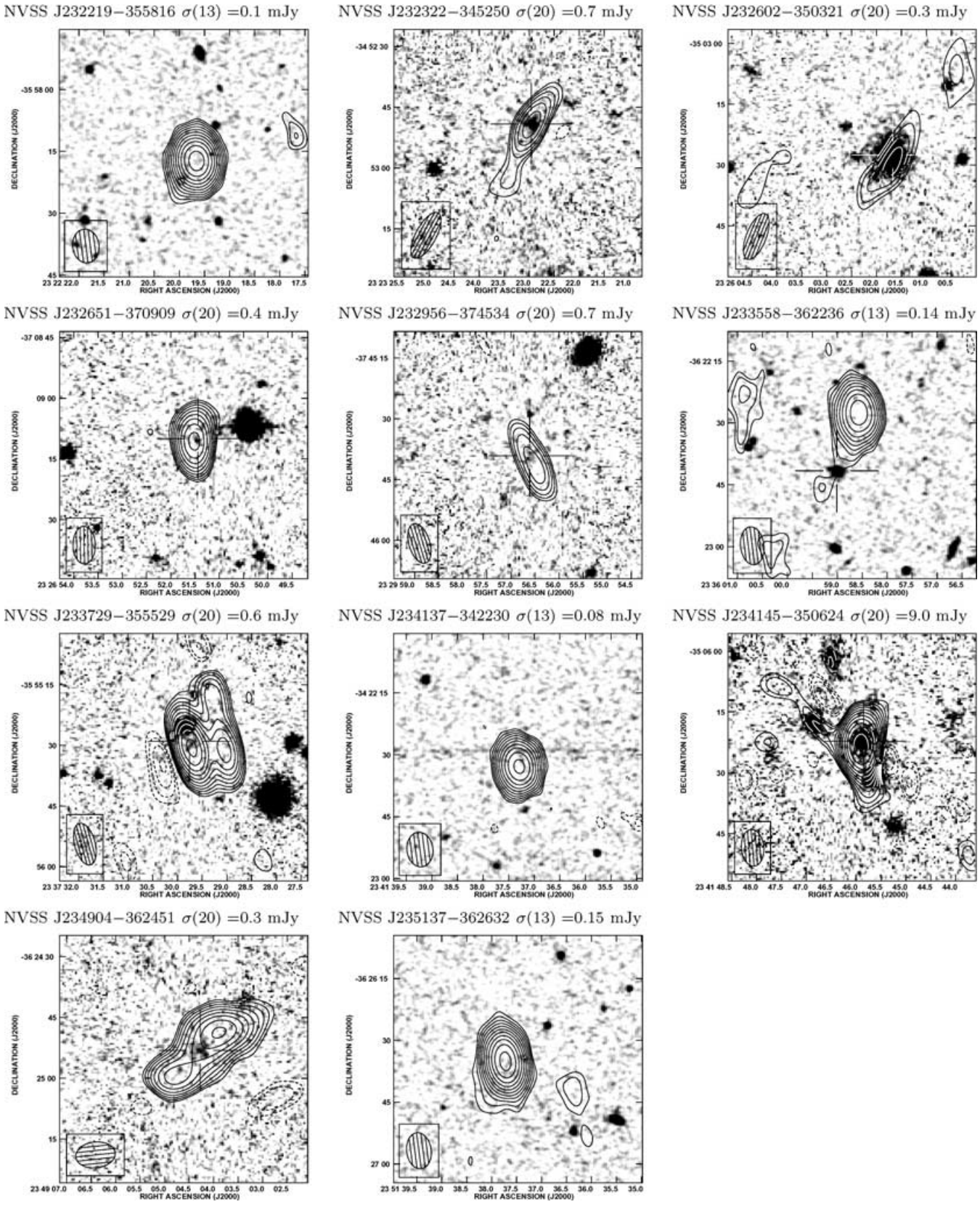

Figure 2 – *continued*

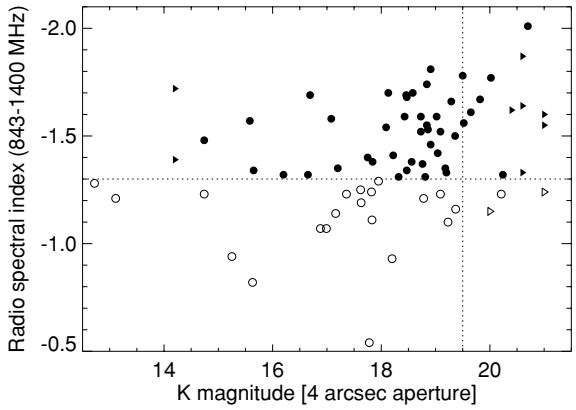

Figure 3. Relation between K magnitude (in a 4-arcsec aperture) and the radio spectral index between 843 MHz and 1.4 GHz. Triangles show upper limits. Filled symbols represent sources with $\alpha_{843}^{1400} < -1.3$, and open symbols those with $\alpha_{843}^{1400} > -1.3$. The vertical dotted line indicates the expected K-band magnitude of a $z \sim 3$ source, and the horizontal dotted line our adopted spectral index cut-off.

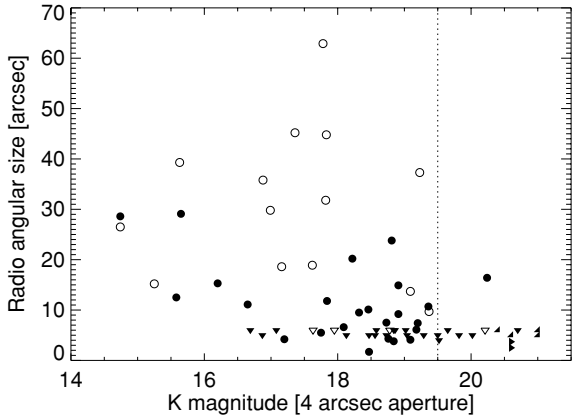

Figure 4. Relation between K magnitude (in a 4 arcsec aperture) of a radio galaxy and the angular size of the radio source. Symbols are as in Fig. 3. The vertical dotted line indicates the expected K-band magnitude of a $z \sim 3$ source. Note the paucity of large radio sources with $K > 19.5$.

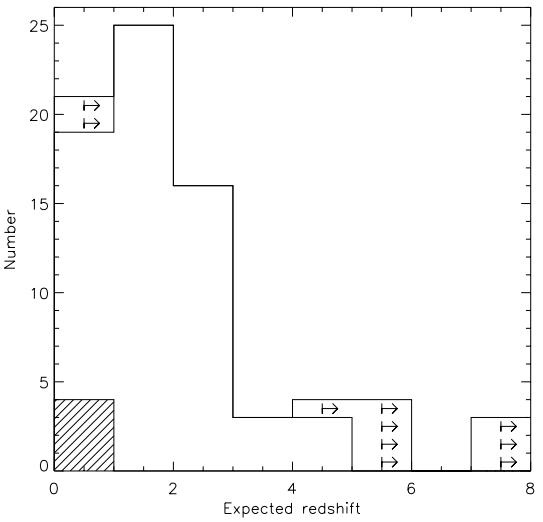

Figure 5. Predicted redshift distribution of the USS sources, estimated from the Hubble K–z diagram. The shaded histogram shows the four sources with spectroscopic redshifts from the 2dFGRS.

the fraction of $z > 3$ radio galaxies in our SUMSS–NVSS USS sample, because the scatter in the α–z relation is quite large.

Table 3 also shows that the fraction of USS sources which have K-band IDs fainter than $K_{64\,\mathrm{kpc}} > 19.5$ mag, making them candidates for very distant ($z > 3$) radio galaxies, appears similar in the SUMSS–NVSS and WENSS–NVSS USS sample with a $S_{1400} > 15$ mJy cut-off. However, the K-band photometry of the WENSS–NVSS USS sample is not complete as most of the WENSS–NVSS sources observed in K-band were pre-selected to be undetected in optical imaging ($R \gtrsim 24$). This preselection will clearly have removed a substantial number of 'intermediate redshift' sources with $K < 19.5$. If the 20 R-band detected sources not observed at K-band are all assumed to have $K < 19.5$, then the fraction decreases to 19.6 per cent, slightly lower than the value found for the SUMSS–NVSS sample.

Thus it appears that spectral index selection between 843 and 1400 MHz is an efficient way of finding distant galaxies, and the full SUMSS–NVSS USS sample should be capable of finding large

Table 3. Surface density of USS sources for different selection methods. Note that these are strictly lower limits due to the incompletenesses in the various USS samples (see text).

Sample	Flux limit (mJy)	Spectral index limit	Area sr	Sources	USS density (sr^{-1})	Fraction of USS with $K > 19.5$ mag	Density (sr^{-1}) USS + $K > 19.5$	Ref.
WENSS–NVSS	$S_{1400} > 10$	$\alpha_{325}^{1400} < -1.3$	2.27	343	151	12/44 (27 per cent)	41 ± 12	1
TEXAS–NVSS	$S_{1400} > 10$	$\alpha_{365}^{1400} < -1.3$	5.58	268	48	8/24 (33 per cent)	16 ± 6	1
MRC–PMN	$S_{408} > 700$	$\alpha_{408}^{4800} < -1.3$	2.23	58	26	0/19	<1.4	1
6C*	$S_{151} > 960$	$\alpha_{151}^{4850} < -0.981$	0.133	24	180	2/24 (8 per cent)	15 ± 11	2
SUMSS–NVSS	$S_{1400} > 15$	$\alpha_{843}^{1400} < -1.3$	0.11	53	482	13/53 (25 per cent)	118 ± 33	3
WENSS–NVSS	$S_{1400} > 15$	$\alpha_{325}^{1400} < -1.3$	2.27	233	103	11/36 (31 per cent)	32 ± 10	1

References: (1) De Breuck et al. (2000, 2002); (2) Blundell et al. (1998), Jarvis et al. (2001); (3) this paper.

numbers of massive galaxies at $z > 3$. Spectroscopy is clearly needed to confirm that the K–z relation holds for these galaxies.

5.3 Expected redshift distribution

We have spectroscopic redshifts of only four sources from the 2dF-GRS. To estimate the redshift distribution of the other 72 sources, we use the Hubble K–z diagram. We have fitted a linear relation to the 64-kpc radio galaxy magnitudes in fig. 7 of De Breuck et al. (2002), yielding $K = 4.633 \log_{10}(z) + 17.266$. To calculate the 64 kpc metric apertures, we used the average correction for $z > 1$, viz. $K_{64\mathrm{kpc}} = K(8\ \mathrm{arcsec}) + 0.2$. Fig. 5 shows the predicted redshift distribution of our sample. The median predicted redshift is 1.75, which is slightly lower than for the WENSS–NVSS and Texas–NVSS USS samples (De Breuck et al. 2002). However, when the optical preselection in the former (see previous section) is taken into account, the SUMSS–NVSS sample has at least as high a median expected redshift.

6 CONCLUSIONS

We have constructed a sample of 76 southern USS sources from the SUMSS and NVSS, including 53 sources with $\alpha_{843}^{1400} < -1.3$. Our ∼5-arcsec resolution radio maps allow the identification of 92 per cent of these sources down to $K \sim 20.5$. The surface density of this SUMSS–NVSS USS sample is more than four times higher than earlier USS samples, which can be explained by a spectral index cut-off which is effectively more relaxed due to the higher selection frequency, and by the use of the same source-finding algorithm in both catalogues. The higher uncertainties in the spectral indices due to the shorter frequency baseline account for a further 35 per cent of $\alpha > -1.3$ source which get scattered into the USS sample.

The distribution of the K-band magnitudes suggests that our sample will be at least as efficient in finding $z > 3$ radio galaxies as earlier USS samples. We intend to obtain full spectroscopic redshift information for this sample to increase the number of potential HzRG targets for follow-up studies with 8-m class telescopes in the southern hemisphere, and to study the radio power dependence in the Hubble K–z diagram out to $z > 3$.

By the end of 2003, SUMSS is expected to cover most of the $\delta < -30^\circ$ region. When combined with the re-analysis of the 408-MHz MRC (Crawford, in preparation), this will allow the construction of a sensitive USS sample at $\delta < -40^\circ$, a region which is virtually unexplored in extragalactic radio astronomy.

ACKNOWLEDGMENTS

We thank the referee Philip Best for his valuable comments, Tom Mauch for useful discussions and Guy Simon for providing the K-band data from the DENIS survey. This publication is based on observations obtained with the Australia Telescope Compact Array, the Anglo-Australian Telescope, and the European Southern Observatory, La Silla, Chile (Program 70.A-0514), and makes use of data products from the Two Micron All Sky Survey, which is a joint project of the University of Massachusetts and the Infrared Processing and Analysis Centre/California Institute of Technology, funded by the National Aeronautics and Space Administration and the National Science Foundation. This work was supported by PICS/CNRS (France) and IREX/ARC (Australia), and by a Marie Curie Fellowship of the European Community programme 'Improving Human Research Potential and the Socio-Economic Knowledge Base' under contract number HPMF-CT-2000-00721.

REFERENCES

Athreya R., Kapahi V., 1998, J. Astrophys. Astr., 19, 63
Blundell K., Rawlings S., Eales S., Taylor G., Bradley A., 1998, MNRAS, 295, 265
Blundell K., Rawlings S., Willott C., 1999, AJ, 117, 677
Bock D., Large M., Sadler E. M., 1999, AJ, 117, 1578
Cavanagh B., Hirst P., Jenness T., Economou F., Currie M. J., Todd S., Ryder S. D., 2003, in Payne H. E., Jedrzejewski R. I., Hook R. N., eds, ASP Conf. Ser. Vol. 295, Astronomical Data Analysis Software and Systems XII. Astron. Soc. Pac., San Francisco, p. 237
Condon J., Cotton W. D., Greisen E. W., Yin Q. F., Perley R. A., Taylor G. B., Broderick J. J., 1998, AJ, 115, 1693
Colless M. et al., 2001, MNRAS, 328, 1039
De Breuck C., van Breugel W., Röttgering H., Miley G., 2000, A&AS, 143, 303
De Breuck C., van Breugel W., Stanford S. A., Röttgering H., Miley G., Stern D., 2002, AJ, 123, 637
De Breuck C. et al., 2003, A&A, 401, 911
Deutsch E. W., 1999, AJ, 118, 1882
Douglas J. N., Bash F. N., Bozyan F. A., Torrence G. W., Wolfe C., 1996, AJ, 111, 1945
Dunlop J., McLure R., Kukula M., Baum S., O'Dea C., Hughes D., 2003, MNRAS, 340, 1095
Dunlop J., 2003, in Ho L. C., ed., Carnegie Obs. Astrophys. Ser. Vol. 1, Coevolution of Black Holes and Glaxies. Cambridge, Cambridge Univ. Press
Epchtein N. et al., 1997, The Messenger, 87, 27
Franceschini A., Vercellone S., Fabian A., 1998, MNRAS, 297, 817
Gillingham P., Jones D., 2000, Proc. SPIE, 4008, 1084
Gopal-Krishna, 1988, A&A, 192, 37
Haehnelt M. G., Kauffmann G., 2001, in Kaper L., van den Heuvel E. P. J., Woudt P. A., eds, Proc. ESO Workshop Black Holes in Binaries and Galactic Nuclei. Springer, Heidelberg, p. 364
Hawarden T., Leggett S., Letawsky M., Ballantyne D., Casali M., 2001, MNRAS, 325, 563
Isobe T., Feigelson E., Nelson P., 1986, ApJ, 306, 490
Jarvis M., Rawlings S., Eales S., Blundell K. M., Bunker A. J., Croft S., McLure R. J., Willott C. J., 2001, MNRAS, 326, 1585
Large M. I., Mills B. Y., Little A. G., Crawford D. F., Sutton J. M., 1981, MNRAS, 194, 693
Lilly S., Longair M., 1984, MNRAS, 211, 833
Loeb A., 1993, ApJ, 403, 542
Mangalam A., Gopal-Krishna, 1995, MNRAS, 275, 976
Mauch T., Murphy T., Buttery H. J., Curran J., Hunstead R. W., Piestrzynski B., Robertson J. G., Sadler E. M., 2003, MNRAS, 342, 1117
Monet D. et al., 1998, USNO-A2.0, VizieR Online Data Catalog. US Naval Observatory, Washington DC, p. 1252 (http://ftp.nofs.navy.mil/projects/pmm/)
Moorwood A., Cuby J., Lidman C., 1998, The Messenger, 91, 9
Murgia M., Fanti C., Fanti R., Gregorini L., Klein U., Mack K.-H., Vigotti M., 1999, A&A, 345, 769
Rengelink R., 1999, PhD thesis, Rijksuniversiteit Leiden
Rengelink R., Tang Y., de Bruyn A. G., Miley G. K., Bremer M. N., Roettgering H. J. A., Bremer M. A. R., 1997, A&AS, 124, 259
Reuland M., van Breugel W., Röttgering H., de Vries W., De Breuck C., Stern D., 2003, ApJ, 582, 71
Sadler E. M., 2003, in Ho L. C., ed., Carnegie Obs. Astrophys. Ser. Vol. 1, Coevolution of Black Holes and Galaxies, available on-line at http://www.ociw.edu/ociw/symposia/series/symposium1/proceedings.html
Skrutskie M. et al., 1997, in Garzon et al., eds, The Impact of Large-Scale Near-IR Sky Surveys. Kluwer, Dordrecht, p. 25
Sohn B., Klein U., Mack K.-H., 2003, A&A, 404, 133
Spergel D. et al., 2003, ApJS, 148, 175
Stern D., Dey A., Spinrad H., Maxfield L., Dickinson M., Schlegel D., González R. A., 1999, AJ, 117, 1122

Tonry J. et al., 2003, ApJ, 594, 1
van Breugel W., De Breuck C., Stanford S. A., Stern D., Röttgering H., Miley G., 1999a, ApJ, 518, L61
van Breugel W. et al., 1999b, in Röttgering H., Best P., Lehnert M., eds, Proc. The Most Distant Radio Galaxies. Royal Netherlands Academy of Arts and Sciences, Amsterdam, p. 49
Venemans B. et al., 2002, ApJ, 569, L11

APPENDIX A: NOTES ON INDIVIDUAL SOURCES

NVSS J001339−322445. This is the northern member of a pair of radio sources separated by 2.2 arcmin on the sky and previously catalogued as PKS 0011-327. While this could be a wide double, we consider it more likely that the two sources are unrelated as there is no plausible optical or near-IR counterpart located between the two sources. The northern (steep–spectrum) source NVSS J001339−322445 is associated with a bright galaxy seen on both the DSS and 2MASS images, and so was not observed with the ATCA or AAT. The southern source, NVSS J001338−322657, has no obvious optical counterpart. Its flux density is 106 mJy in NVSS and 141 mJy in SUMSS, giving a spectral index of −0.56.

NVSS J002001−333408. The *K*-band identification is located at the centre of the extended radio source.

NVSS J002112−321208. The diffuse *K*-band identification is offset by $(\Delta\alpha, \Delta\delta) = (2.0$ arcsec W, 1.5 arcsec S) from the ATCA position.

NVSS J002131−342225. The source is identified with the (uncatalogued) bright galaxy located between the radio lobes.

NVSS J002219−360728. An optical galaxy is clearly visible on the digitized sky survey images at the NVSS position, so this source was not observed with the ATCA or AAT.

NVSS J002352−332338. We identify the host galaxy with the faint *K*-band object located along the radio axis, offset by $(\Delta\alpha, \Delta\delta) = (7.6$ arcsec E, 3.4 arcsec N) from the NVSS position.

NVSS J002359−325756. The *K*-band identification is located in between the radio lobes. This source is also known as PMN J0024−3258.

NVSS J002402−325253. The diffuse *K*-band identification is offset by $(\Delta\alpha, \Delta\delta) = (0.6$ arcsec W, 1.1 arccsec N) from the ATCA position.

NVSS J002415−324102. The diffuse *K*-band identification is located at the ATCA position.

NVSS J002427−325135. The *K*-band identification is located in between the radio lobes.

NVSS J002627−323653. An optical galaxy is clearly visible on the digitized sky survey images at the NVSS position, so this source was not observed with the ATCA or AAT.

NVSS J002738−323501. The diffuse *K*-band identification is located at the midpoint of the radio lobes.

NVSS J011032−335445. The *K*-band identification is located at the ATCA position.

NVSS J011606−331241. The *K*-band identification is located at the ATCA position.

NVSS J011643−323415. We identify the compact *K*-band source offset by $(\Delta\alpha, \Delta\delta) = (0.5$ arcsec W, 3.6 arcsec S) from the NVSS position.

NVSS J012904−324815. This bright source is clearly detected in 2MASS using the NVSS astrometry. We therefore did not observe it with the ATCA or AAT.

NVSS J014413−330457. This radio source has a complex morphology. We identify a diffuse *K*-band source at the position of the brightest radio component, which is most likely the core. In Table 1, we list the position of this radio core.

NVSS J014529−325915. The diffuse radio source appears to lie within a small a cluster of galaxies. We identify the bright *K*-band source offset by $(\Delta\alpha, \Delta\delta) = (2.6$ arcsec E, 2.0 arcsec S) from the ATCA position.

NVSS J015223−333833. The *K*-band identification is located along the radio axis, offset by $(\Delta\alpha, \Delta\delta) = (1.6$ arcsec E, 2.7 arcsec S) from the midpoint between the radio lobes in the ATCA image.

NVSS J015232−333952. The bright *K*-band identification is located between the main two radio lobes. The radio source, also known as PMN J0152−3340, has a complex morphology with a fainter lobe to the east of the main two radio lobes.

NVSS J015324−334117. The diffuse radio source appears to lie within a small a cluster of galaxies. We identify the bright *K*-band source offset by $(\Delta\alpha, \Delta\delta) = (6.4$ arcsec E, 6.7 arcsec S) from the ATCA position.

NVSS J015418−330150. The faint *K*-band identification is located at the ATCA position.

NVSS J015436−333425. The diffuse *K*-band identification is located at the ATCA position.

NVSS J015544−330633. The bright *K*-band identification is located between the radio lobes.

NVSS J021308−322338. The *K*-band identification is located at the ATCA position.

NVSS J021359−321115. The *K*-band identification is located at the ATCA position.

NVSS J021545−321047. The *K*-band identification is located along the radio axis, offset by $(\Delta\alpha, \Delta\delta) = (1.4$ arcsec W, 0.2 arcsec S) from the midpoint between the radio lobes in the ATCA image.

NVSS J021716−325121. The *K*-band identification is located between the radio lobes.

NVSS J030639−330432. The *K*-band identification is located at the ATCA position. This source is also known as TXS 0304−332.

NVSS J202026−372823. The *K*-band identification is located at the ATCA position.

NVSS J202140−373942. The *K*-band identification is located at the central of the three radio components.

NVSS J202518−355834. The *K*-band identification is located at the ATCA position.

NVSS J202856−353709. The bright *K*-band identification is located between the radio lobes.

NVSS J202945−344812. The *K*-band identification is located along the radio axis, offset by $(\Delta\alpha, \Delta\delta) = (1.7$ arcsec E, 5.0 arcsec S) from the midpoint between the radio lobes in the ATCA image.

NVSS J204147−331731. The bright *K*-band identification is located between the radio lobes.

NVSS J204420−334948. No *K*-band source is seen near the radio position in our medium deep SofI image.

NVSS J213510−333703. The faint *K*-band identification is located at the ATCA position.

NVSS J225719−343954. The bright *K*-band identification is located at the ATCA position. The bright galaxy south of the ATCA position has $z = 0.0871$ from the 2dFGRS.

NVSS J230035−363410. The very faint *K*-band identification is offset by $(\Delta\alpha, \Delta\delta) = (1.4$ arcsec E, 1.6 arcsec S) from the ATCA position.

NVSS J230123−364656. The faint *K*-band identification is located at the ATCA position.

NVSS J230203−340932. The K-band identification is located near the central radio component, which is most likely the core. In Table 1, we list the position of this radio core.

NVSS J230404−372450. The K-band identification is located between the radio lobes.

NVSS J230527−360534. No K-band source is seen near the radio position in our SofI image.

NVSS J230822−325027. The K-band identification is located at the ATCA position.

NVSS J230846−334810. The radio source has a complex morphology, consisting of at least four components. The K-band identification is surrounded by a number of fainter clumps. This source resembles WN J1015+3038 and TN J1049−1258 (De Breuck et al. 2002).

NVSS J230954−365653. There are several faint K-band sources located in between the radio lobes. A deeper radio map would be needed to determine with certainty which one is the host galaxy. We tentatively identify the galaxy closest to the line connecting the radio lobes.

NVSS J231016−363624. The bright K-band identification is located between the radio lobes. This source is also detected in the DENIS survey with $K = 14.197$ in a 4.5-arcsec aperture.

NVSS J231144−362215. The very faint K-band identification is located between the radio lobes.

NVSS J231229−371324. The K-band identification is located at the ATCA position.

NVSS J231311−361558. The K-band identification is located at the midpoint of the radio lobes. This is the largest radio source in our sample.

NVSS J231317−352133. The position quoted in Table 1 is for the bright eastern component only, because the K-band identification coincides with this lobe.

NVSS J231335−370609. The K-band identification is offset by $(\Delta\alpha, \Delta\delta) = (0.3$ arcsec E, 1.9 arcsec N) from the ATCA position.

NVSS J231338−362708. The faint K-band identification is located between the radio lobes.

NVSS J231341−372504. The K-band identification is located at the midpoint of the radio lobes.

NVSS J231357−372413. The K-band identification is located at the ATCA position.

NVSS J231402−372925. The K-band identification is located at the ATCA position.

NVSS J231459−362859. The K-band identification is located at the ATCA position.

NVSS J231519−342710. The K-band identification is located along the radio axis, offset by $(\Delta\alpha, \Delta\delta) = (5.9$ arcsec E, 2.1 arcsec S) from the midpoint between the radio lobes in the ATCA image.

NVSS J231726−371443. There are two K-band objects located along the radio axis, which may both be components of the host galaxy. We conservatively assume that only the northernmost component, offset by $(\Delta\alpha, \Delta\delta) = (0.2$ arcsec E, 2.2 arcsec S) from the northern radio lobe in the ATCA image, is the host galaxy. The position quoted in Table 1 is for the bright northern component only, because it is near the NVSS position.

NVSS J231727−352606. No K-band source is seen near the radio position in our medium deep SofI image.

NVSS J232001−363246. The faint K-band identification is located at the ATCA position.

NVSS J232014−375100. The K-band identification is located between the radio lobes of this large radio source, offset by $(\Delta\alpha, \Delta\delta) = (4.1$ arcsec W, 0.1 arcsec S) from the NVSS position.

NVSS J232058−365157. The K-band identification is located at the ATCA position.

NVSS J232100−360223. The very faint K-band identification is offset by $(\Delta\alpha, \Delta\delta) = (1.2$ arcsec W, 1.1 arcsec N) from the ATCA position.

NVSS J232219−355816. No K-band source is seen near the radio position in our SofI image.

NVSS J232322−345250. The K-band identification is located at the ATCA position.

NVSS J232408−353547. An optical galaxy is seen in both the DSS and 2MASS at the NVSS position, so we did not observe this source with the ATCA or AAT.

NVSS J232602−350321. The bright K-band identification is coincident with an extended radio source.

NVSS J232651−370909. The faint K-band identification is located at the ATCA position.

NVSS J232956−374534. The faint K-band identification is offset by $(\Delta\alpha, \Delta\delta) = (0.7$ arcsec E, 1.5 arcsec N) from the ATCA position.

NVSS J233558−362236. We identify the host galaxy as the bright K-band source, located along the radio axis, nearer to the brightest radio lobe.

NVSS J233729−355529. The radio source has a complex morphology, consisting of three non-aligned components. We identify the host galaxy with a diffuse K-band source, coincident with the brightest radio component.

NVSS J234137−342230. No K-band source is seen near the radio position in our SofI image.

NVSS J234145−350624. The bright K-band identification is located at the ATCA position. This source is also known as PKS J2341−3506.

NVSS J234904−362451. The K-band identification is located between the radio lobes.

NVSS J235137−362632. No K-band source is seen near the radio position in our medium deep SofI image.

This paper has been typeset from a TEX/LATEX file prepared by the author.